

Quantum nondemolition gate operations and measurements in real time on fluctuating signals

Yu Shiozawa,¹ Jun-ichi Yoshikawa,¹ Shota Yokoyama,^{1,2} Toshiyuki Kaji,¹ Kenzo Makino,¹ Takahiro Serikawa,¹ Ryosuke Nakamura,¹ Shigenari Suzuki,¹ Shota Yamazaki,¹ Warit Asavanant,¹ Shuntaro Takeda,^{1,3} Peter van Loock,⁴ and Akira Furusawa^{1,*}

¹*Department of Applied Physics, School of Engineering, The University of Tokyo, 7-3-1 Hongo, Bunkyo-ku, Tokyo 113-8656, Japan*

²*Centre for Quantum Computation and Communication Technology, School of Engineering and Information Technology, University of New South Wales Canberra, ACT 2600, Australia*

³*JST, PRESTO, 4-1-8 Honcho, Kawaguchi, Saitama 332-0012, Japan*

⁴*Institute of Physics, Johannes Gutenberg-Universität Mainz, Staudingerweg 7, 55099 Mainz, Germany*



(Received 26 December 2017; published 9 November 2018)

We demonstrate an optical quantum nondemolition (QND) interaction gate with a bandwidth of about 100 MHz. Employing this gate, we are able to perform QND measurements in real time on randomly fluctuating signals. Our QND gate relies on linear optics and offline-prepared squeezed states. In contrast to previous demonstrations on narrow sideband modes, our gate is compatible with quantum states temporally localized in a wave-packet mode including non-Gaussian quantum states. This is the cornerstone of realizing quantum error correction and universal gate operations.

DOI: [10.1103/PhysRevA.98.052311](https://doi.org/10.1103/PhysRevA.98.052311)

I. INTRODUCTION

Quantum information processing with light is a promising approach for universal and scalable quantum computation. In recent years, there has been significant progress in optical continuous variable (CV) quantum computation by using a time-domain multiplexing scheme [1–4], where quantum states are encoded in a string of wave-packet modes in a single optical beam. This scheme enables us to prepare an unlimited number of quantized modes in a single beam, individually access each of these modes, and continuously manipulate these modes with a small number of optical components. Therefore, this is one of the most efficient and practical schemes in terms of scalability and, in practice, the largest-scale entangled quantum state to date was generated by the time-domain multiplexing scheme [4]. Although such entanglement, in principle, enables universal and large-scale quantum computation, error correction to achieve fault tolerance and non-Gaussian gate operations [5] still remain big challenges for CV quantum computation with time-domain multiplexing schemes.

To realize error correction and non-Gaussian operations, a quantum nondemolition (QND) interaction [6–8], which couples two quantum systems, is an essential component. A QND gate is indispensable to error syndrome measurements [9–11], including the special case of CV error correction schemes [5,12–14], and also required for non-Gaussian operations via gate teleportation [5,15]. In one of the previous demonstrations, a QND gate using linear optics and offline prepared squeezed states was demonstrated with high precision [16,17]. This off-line scheme can, in principle, be applied to an arbitrary optical quantum state. However, QND gates in the previous demonstrations [17–19] only work on

quantum states in narrow sideband modes in the frequency domain. This means that these gates are not applicable to general quantum states generated in wave-packet modes and not compatible with the time-domain multiplexing schemes. Therefore, a broadband QND gate which can work on wave-packet modes needs to be implemented for fault-tolerant and universal quantum computation with the time-domain multiplexing schemes.

In this paper, we demonstrate QND gate operations and measurements on continuously fluctuating signals in real time with a bandwidth of about 100 MHz. Unlike previous experiments [17–19], the input signal is randomly fluctuating with a short autocorrelation time, and thus the success of QND interactions on this signal is a proof that our gate correctly operates instant signals without memory-like effects. The time-domain traces of quadrature values are obtained in real time by just applying electric filters [20], and thus can be interpreted as results of real-time QND measurements with respect to time-shifted wave-packet modes determined by the electric filters. Since our QND gate works on any wave-packet mode for up to about 100 MHz, our gate is compatible with general quantum states including non-Gaussian quantum states such as single-photon states [21,22] and Schrödinger’s cat states [23,24], which are included in many CV protocols [5,25,26]. Note that, for CV single-mode squeezing and teleportation gates, operations on such non-Gaussian quantum states have already been demonstrated with a bandwidth of about 10 MHz [27–32]. Here we demonstrate a broadband *interaction* gate, and furthermore the bandwidth is widened to about 100 MHz. Our gate is a crucial component for future realizations of error correction schemes [5,12–14] based on the time-domain multiplexing and non-Gaussian gate operations which are necessary for universal quantum computation [5,15,25,26]. In addition, our gate is also applicable to generate time-domain multiplexed cluster states for one-way quantum computation

*akiraf@ap.t.u-tokyo.ac.jp

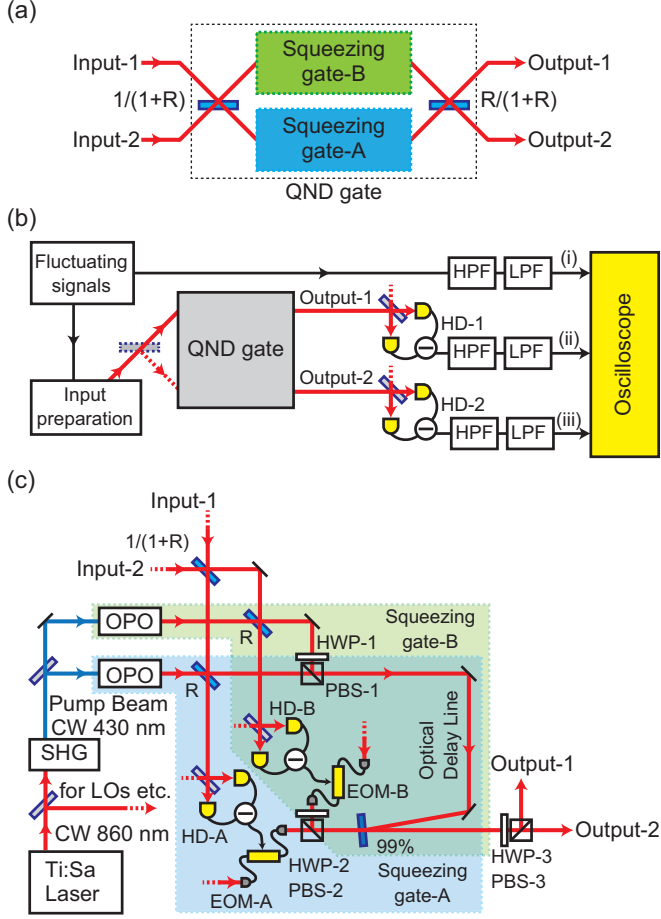


FIG. 1. Experimental setup. (a) Decomposition of a QND gate. (b) Peripheral systems for the input signal preparation and the output measurements. Input optical signal is sent to either Input 1 or Input 2. (c) Experimental setup of the QND gate. Squeezing gates A and B share an optical delay line in orthogonal polarizations. “SHG” labels a second-harmonic generator; “HD” labels a homodyne detector.

[1,33], to employ CV gate sequences in a loop-based architecture [34] and for CV coherent communication [35].

II. THEORY

Let us define quadratures of a quantum optical field mode k as \hat{x}_k and \hat{p}_k with $\hat{x}_k \equiv (\hat{a}_k^\dagger + \hat{a}_k)$ and $\hat{p}_k \equiv i(\hat{a}_k^\dagger - \hat{a}_k)$, where \hat{a}_k and \hat{a}_k^\dagger are annihilation and creation operators, respectively ($\hbar = 2$, $[\hat{x}_k, \hat{p}_{k'}] = 2i\delta_{kk'}$). The QND interaction is a two-mode unitary operation $\hat{U}_{\text{QND}} = \exp(-\frac{i}{2}G\hat{x}_1\hat{p}_2)$, where G is a QND gain, i.e., the strength of the interaction of two optical modes. This interaction transforms the quadrature operators as

$$\begin{bmatrix} \hat{x}_1^{\text{out}} \\ \hat{x}_2^{\text{out}} \end{bmatrix} = \begin{bmatrix} 1 & 0 \\ G & 1 \end{bmatrix} \begin{bmatrix} \hat{x}_1^{\text{in}} \\ \hat{x}_2^{\text{in}} \end{bmatrix}, \quad \begin{bmatrix} \hat{p}_1^{\text{out}} \\ \hat{p}_2^{\text{out}} \end{bmatrix} = \begin{bmatrix} 1 & -G \\ 0 & 1 \end{bmatrix} \begin{bmatrix} \hat{p}_1^{\text{in}} \\ \hat{p}_2^{\text{in}} \end{bmatrix}. \quad (1)$$

Since the QND interaction belongs to the class of Gaussian operations, it is decomposable into beam-splitter interactions and single-mode squeezing operations [see Fig. 1(a)] [16,36]. Furthermore, squeezing is also a Gaussian operation and

is realized by an off-line scheme with a beam splitter and ancillary squeezed light [16], where the squeezing degree is tunable via the reflectivity of the beam splitter R . The QND gate is implemented by choosing the beam-splitter reflectivities before and after the squeezing gates as $1/(1+R)$ and $R/(1+R)$, respectively [see Fig. 1(a)]. We obtain

$$\hat{x}_1^{\text{out}} = \hat{x}_1^{\text{in}} - \sqrt{\frac{1-R}{1+R}} \hat{x}_A^{(0)} e^{-r_A}, \quad (2a)$$

$$\hat{x}_2^{\text{out}} = \frac{1-R}{\sqrt{R}} \hat{x}_1^{\text{in}} + \hat{x}_2^{\text{in}} + \sqrt{R \frac{1-R}{1+R}} \hat{x}_A^{(0)} e^{-r_A}, \quad (2b)$$

$$\hat{p}_1^{\text{out}} = \hat{p}_1^{\text{in}} - \frac{1-R}{\sqrt{R}} \hat{p}_2^{\text{in}} + \sqrt{R \frac{1-R}{1+R}} \hat{p}_B^{(0)} e^{-r_B}, \quad (2c)$$

$$\hat{p}_2^{\text{out}} = \hat{p}_2^{\text{in}} + \sqrt{\frac{1-R}{1+R}} \hat{p}_B^{(0)} e^{-r_B}, \quad (2d)$$

where $\hat{x}_A^{(0)} e^{-r_A}$ and $\hat{p}_B^{(0)} e^{-r_B}$ are quadratures of ancillary squeezed vacua of squeezing gates A and B with finite squeezing parameters r_A and r_B . In the ideal limit of $r_A, r_B \rightarrow \infty$, both $\hat{x}_A^{(0)} e^{-r_A}$ and $\hat{p}_B^{(0)} e^{-r_B}$ terms vanish, and Eq. (2) becomes equivalent to Eq. (1), where the QND gain is $G = (1-R)/\sqrt{R}$. In the experiment, we choose the QND gain $G = 1$. In this case, $R = (3 - \sqrt{5})/2 \approx 0.38$, $1/(1+R) \approx 0.72$, and $R/(1+R) \approx 0.28$.

For characterization of the gate, we obtain the quadratures \hat{x}_k or \hat{p}_k ($k = 1, 2$) by homodyne detection by using a local oscillator (LO). Generally, in the case that the LO is a continuous coherent light, the detected homodyne signal is also continuous. The quadrature of a quantum state in a wave-packet mode $g_{\text{mode}}(t)$ is obtained from the original homodyne signal $\hat{X}_k(t)$ by an integration $\hat{x}_k = \int g_{\text{mode}}(\tau) \hat{X}_k(\tau) d\tau$. On the other hand, when a continuous signal $\hat{X}_k(t)$ passes through a filter with a response function $g_{\text{filter}}(t)$, the resulting continuous signal becomes $\hat{x}_k(t) = \int g_{\text{filter}}(t - \tau) \hat{X}_k(\tau) d\tau$. Therefore we obtain quadrature values in real time just by inserting an electric filter, where the mode function that corresponds to the quadrature value $\hat{x}_k(t_0)$ obtained at time t_0 is $g_{\text{mode}, t_0}(t) = g_{\text{filter}}(t_0 - t)$ [20]. Note that real-time measurements are necessary for nonlinear feed-forward operations in measurement-based quantum computation [20]. We choose a low-pass filter (LPF) which has a flat passband and a steep edge with a cutoff frequency of 100 MHz to treat the bandwidth of 100 MHz equally. However, the QND gate itself can work on arbitrary wave-packet modes for up to the bandwidth of 100 MHz, enabling operations on non-Gaussian states.

As already noted, to show memoryless features of our gate, we use random white signals as inputs. From the signal-to-noise ratio of this random signal, we can evaluate the conventional QND quantities T_S and T_P [37]. However, unlike previous experiments [7,8,17–19], it may not be appropriate to evaluate T_S and T_P just by transfer of signal powers. If the signal is modified unexpectedly by irregular gate responses, a part of the input signal is considered to be converted to noise at the output, by which the effective T_S and T_P degrades. To exclude such a possibility, we check the cancellation of the output signals by using the input signal. The setup is shown in Fig. 1(b). The random signal is split into two; one is

utilized for generating the input optical signal, and the other is stored for reference. Here we set the target of the QND measurement to the quadrature amplitude produced by the random signal in the wave-packet mode defined by the electric filters. This input amplitude is directly stored by applying the same electric filters to the random signal before storage. Therefore, we can cancel the produced output signals [(ii) and (iii) in Fig. 1(b)] by using the stored signal [(i) in Fig. 1(b)] with an appropriate shift of the time origin. This is also an achievement of this research.

III. EXPERIMENTAL SETUP

We use a continuous-wave (cw) Ti:sapphire laser at a wavelength of 860 nm. Input states of the QND gate are vacuum states and coherent states. We generate a random optical signal by using a waveguide electro-optics modulator (EOM) and amplified Johnson electric noise, which is applied to each of the input quadratures (x_1^{in} , x_2^{in} , p_1^{in} , p_2^{in}). For the frequency characteristic of the random signal and the scheme of generating the coherent state, see Appendix A. The other three input quadratures are at vacuum levels. This is sufficient to characterize the gate-response matrix on the assumption of the linearity of the gate.

The QND gate consists of a Mach-Zehnder interferometer containing two squeezing gates in it as shown in Fig. 1(a). The squeezing gate has an optical delay line to compensate the delay of electronic circuits for feed-forward operations. To match the delays of two squeezing gates, we implement a common delay line (about 3 m) by utilizing the optical polarization degrees of freedom as shown in Fig. 1(c). We insert a half-wave plate (HWP) before a polarizing beam splitter (PBS) to separate the two outputs, by which the latter beam splitter $R/(1+R)$ is implemented. The ancillary squeezed vacua are generated from triangle-shaped optical parametric oscillators (OPOs) [38]. For the broadband spectra of ancillary squeezed vacua and homodyne detectors, see Appendix A.

We apply, in addition to the 100 MHz LPF mentioned above, a high-pass filter (HPF) with a cutoff frequency of 1 MHz to the output homodyne signals for rejection of low-frequency noise. The mode function is mainly determined by the LPF, and the deformation of it by the HPF is negligible. We acquire the filtered homodyne signals, together with the filtered input signal, by an oscilloscope at the sampling rate of 1 GHz. For the QND quantities T_S , T_P , and $V_{S|P}$ [37], we use 1000 sets of sequential 10 000 data points. For the power spectra, we use 9000 sets of sequential 1024 data points.

IV. EXPERIMENTAL RESULTS

First, as an example, we show the time-domain traces for the case where the white signal is applied to \hat{x}_1^{in} . The other three cases are shown in Appendix B. In Fig. 2, we show typical time-domain traces of the filtered white signals and the filtered homodyne signals for 300 ns. Figures 2(a) and 2(b) show the traces of the input white signal and the output quadratures \hat{x}_1^{out} and \hat{x}_2^{out} [(i), (ii), and (iii) in Fig. 1(b)], respectively. We can see that the output quadratures \hat{x}_1^{out} and \hat{x}_2^{out} follow the input white signal with a time delay of 36 ns, which is shown by gray backgrounds and dotted lines in Figs. 2(a) and 2(b). This

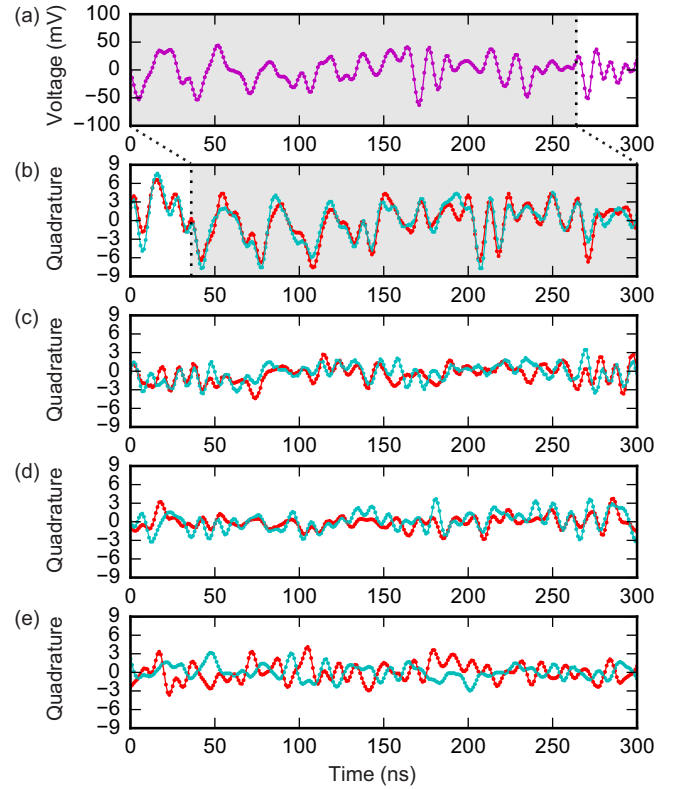


FIG. 2. Time-domain traces for 300 ns. (a) The filtered input white signals. (b) The filtered output homodyne signals: red (gray) is \hat{x}_1^{out} ; cyan (light gray) is \hat{x}_2^{out} . (c) Results of the cancellation: red (gray) is \hat{x}_1^{out} ; cyan (light gray) is \hat{x}_2^{out} . (d) The filtered output homodyne signals for vacuum inputs: red (gray) is \hat{x}_1^{out} ; cyan (light gray) is \hat{x}_2^{out} . (e) The filtered output homodyne signals for vacuum inputs: red (gray) is \hat{p}_1^{out} ; cyan (light gray) is \hat{p}_2^{out} .

means that the signal input \hat{x}_1^{in} is transmitted nondestructively to the signal output \hat{x}_1^{out} , and simultaneously the signal information is copied to the probe output \hat{x}_2^{out} . Then we subtract the input white signal from the output respective quadratures \hat{x}_1^{out} and \hat{x}_2^{out} with an optimum gain and the time shift; the results are shown in Fig. 2(c). As references, in Fig. 2(d), we also show traces of \hat{x}_1^{out} and \hat{x}_2^{out} for the case of vacuum input. We can see that the variances of the residual fluctuations in Fig. 2(c) are comparable to those of the vacuum input case in Fig. 2(d). The nice cancellation with a simple time shift means that the gate converts the instant input signals to the instant output signals without memory-like effects in this timescale. Without the added random signals, there is still some positive correlation independent of the input signal in \hat{x}_1^{out} and \hat{x}_2^{out} . On the other hand, when we look at \hat{p}_1^{out} and \hat{p}_2^{out} in Fig. 2(e), there is a negative correlation. Figures 2(d) and 2(e) show the quantum entanglement generated by the gate interaction.

Next, to evaluate the cancellation more precisely, we apply a Fourier transform to the results; the resulting power spectra are shown in Fig. 3. The spectra for the vacuum-state input, the coherent-state input, the cancellation, and the homodyne shot noise as a reference are colored in red, magenta, green, and black, respectively. In the case of an ideal QND interaction of vacuum inputs with $G = 1$, \hat{x}_1^{out} and \hat{p}_2^{out} are kept

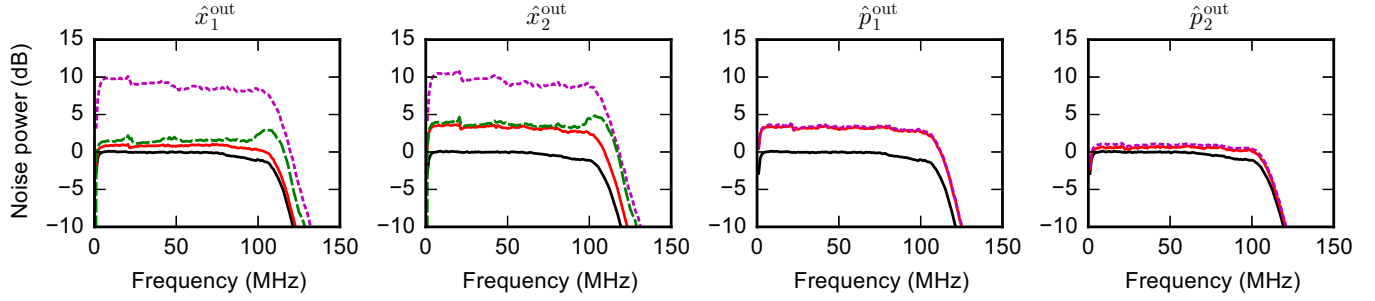


FIG. 3. Power spectra of output quadratures when a random signal is added to \hat{x}_1^{in} . Black (bottom) shows shot noise. Red shows results of vacuum-state input. Dotted magenta shows results of coherent-state input. Dashed green shows cancellation of the random signal.

at the shot-noise level, while \hat{x}_2^{out} and \hat{p}_1^{out} are increased by 3 dB from the shot-noise level, because a vacuum fluctuation of \hat{x}_1^{in} or \hat{p}_2^{in} is added. Our results are in good agreement with this, although there is some excess noise increase due to finite squeezing of ancillary states. When the input white signal is added to \hat{x}_1^{in} , the powers of \hat{x}_1^{out} and \hat{x}_2^{out} increase by the same amount, showing the unity gain of the QND interaction, while those of \hat{p}_1^{out} and \hat{p}_2^{out} do not increase, showing negligible crosstalk between x and p quadratures. Comparing the vacuum-input (red) trace and the signal-canceled (dashed green) trace, we can see that the cancellation is almost perfectly working for up to about 100 MHz. Further discussions of the cancellations by introducing response functions are included in Appendix B.

Finally, we evaluate the QND quantities T_S , T_P , and V_{SIP} for both \hat{x} and \hat{p} quadratures (see Appendix C). The success of QND measurements is commonly verified by the

criteria [37]

$$1 < T_S + T_P, \quad V_{\text{SIP}} < 1. \quad (3)$$

The experimentally determined values are $T_S + T_P = 1.37 \pm 0.03 > 1$ and $V_{\text{SIP}} = 0.88 \pm 0.01 < 1$ for the \hat{x} quadratures, and $T_S + T_P = 1.37 \pm 0.03 > 1$ and $V_{\text{SIP}} = 0.88 \pm 0.01 < 1$ for the \hat{p} quadratures. Therefore, we succeeded in constructing a QND gate that enables real-time QND measurements for both conjugate quadratures with the bandwidth of about 100 MHz. For a more detailed analysis, we show the QND quantities at each frequency in Fig. 4. All of T_S , T_P , and V_{SIP} satisfy the QND criteria up to about 100 MHz. As for V_{SIP} , because of the finite bandwidth of the ancillary squeezed vacua, the correlation degrades at higher frequencies; however, there are still sub-shot-noise correlations for up to about 100 MHz. The two output modes are entangled, which is described in Appendix D.

V. CONCLUSIONS

We experimentally demonstrated an optical two-mode QND interaction gate that enables real-time QND measurements on temporally fluctuating random signals. We also showed that the interaction works over a broad spectrum; namely, up to about 100 MHz in the frequency domain. The capability of the gate to deal with instantaneous signals is confirmed by the cancellation of random signals. The realization of a broadband QND gate paves the way for achieving fault-tolerant universal quantum computation with the time-domain multiplexing schemes and many CV quantum protocols.

ACKNOWLEDGMENTS

This work was partly supported by CREST (JPMJCR15N5) and PRESTO (JPMJPR1764) of JST, JSPS KAKENHI, APSA. P.v.L. was supported by Qcom (BMBF). Y.S., S.Y., and T.S. acknowledge financial support from ALPS.

APPENDIX A: DETAILED EXPERIMENTAL SETUP AND FREQUENCY SPECTRA

1. Electric filters and response function

The homodyne signals for verification as well as the white signals for the QND input are stored by an oscilloscope (DPO7054, Tektronix) after a low-pass filter (LPF) and a

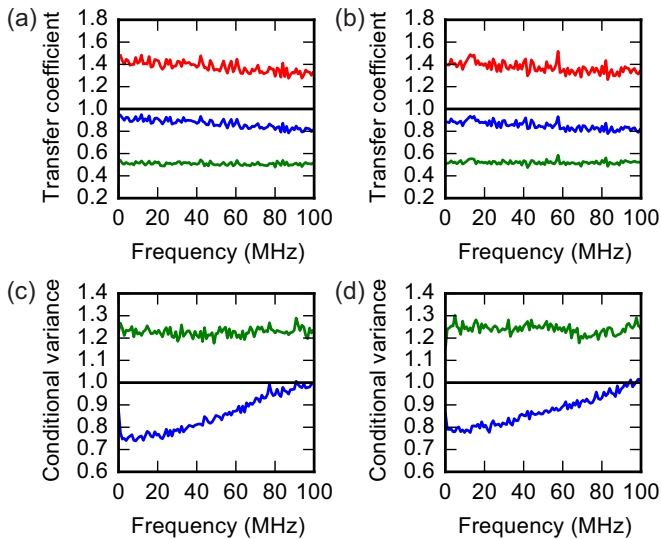


FIG. 4. Spectra of the QND quantities. (a), (b) Transfer coefficients when the random signal is added to \hat{x}_1^{in} or \hat{p}_1^{in} , respectively. Red (top), blue (middle), and green (bottom) traces are $T_S + T_P$, T_S , and T_P respectively. (c), (d) Conditional variances for vacuum inputs, i.e., the variances of $\hat{x}_1^{\text{out}} - g_x \hat{x}_2^{\text{out}}$ and $g_p \hat{p}_1^{\text{out}} + \hat{p}_2^{\text{out}}$ at the gain $g_x = 0.41$ and $g_p = 0.39$, respectively (see Appendix D), normalized by the shot noise spectrum. Blue (bottom) and green (top) traces are for the cases with and without the ancillary squeezed vacua, respectively.

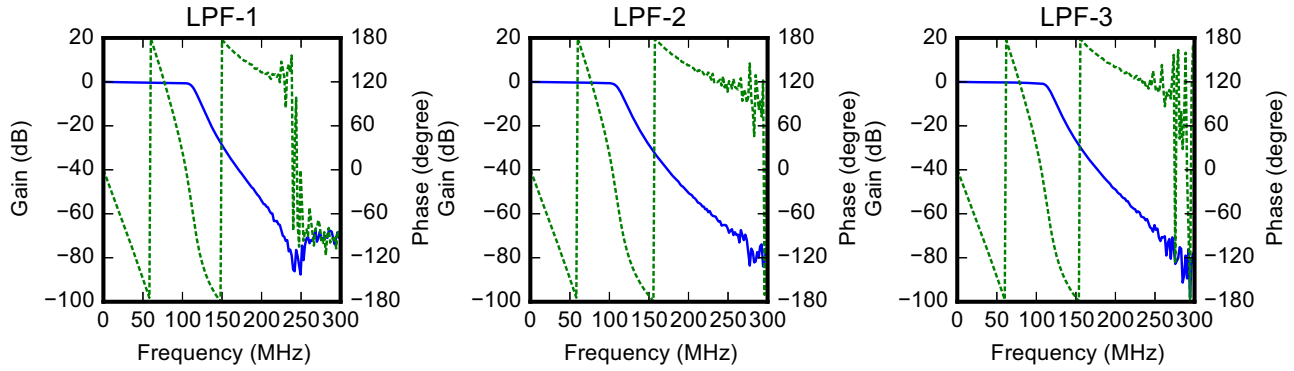


FIG. 5. Frequency characteristics of the LPFs, obtained by a network analyzer (Keysight, E5061B). Blue is gain, dotted green is phase.

high-pass filter (HPF). The LPF is a commercially available filter whose cutoff frequency is 100 MHz (Mini-Circuits, BLP-100+). We plot the frequency characteristics of the LPF in Fig. 5. The HPF is a homemade first-order filter with a cutoff frequency of 1 MHz, which is used to remove low-frequency noise around the laser carrier frequency. We plot the frequency characteristics of the HPF in Fig. 6. The mode function $g_{\text{mode}}(t)$ is mainly determined by the LPF. The time-domain response function $g_{\text{filter}}(t)$ calculated from the gain and phase in Fig. 5 is shown in Fig. 7. As mentioned in the main text, the time-reversal response function with time shifts is the effective mode function $g_{\text{mode}}(t)$ for the QND measurements.

2. White signal source

Figure 8 shows the power spectrum of the white signal used for the input of the QND gate. The white signal is amplified thermal noise from resistors and operational amplifiers (OPA847, Texas Instruments). The trace in green represents unfiltered signals, while the trace in blue represents filtered signals which corresponds to the signals stored by the oscilloscope in the actual QND experiment.

3. Homodyne detectors

Figure 9 shows the optical shot-noise spectra with a local oscillator (LO) power of 10 mW, together with the detector dark noise spectra, of the four homodyne detectors (two for feed-forward operations and two for QND measurements). We

show both the filtered and unfiltered cases. The shot-noise spectra are flat up to about 100 MHz for all of the four detectors. The clearance between the shot noise and the dark noise is more than 10 dB even at 100 MHz.

4. Ancillary squeezed vacua

Figure 10 shows the power spectra of the squeezed and antisqueezed quadratures of the ancillary squeezed vacua normalized by the shot noise spectrum. The power of the pump beam is 85 mW. Both of the two squeezed vacua show about -5 dB of squeezing at low frequencies and about -2 dB of squeezing at 100 MHz. These spectra are in good agreement with the bandwidths of the OPO cavities (about 150 MHz of full width at half maximum).

5. Control of optical systems

To lock interference phases in the QND gate, we use weak laser beams as phase references for each optical paths. These reference beams are temporally turned on and off by switching a pair of acousto-optic modulators (AOMs). We control the optical systems by feedback when the reference beams are on, while the system is held and the QND gate is tested when they are off. The duration of ON time is $1400 \mu\text{s}$ and that of OFF time is $600 \mu\text{s}$. The QND measurement data are acquired within $10 \mu\text{s}$ in the OFF time, during which the drift of the optical system is negligible.

However, there are some beams which cannot be turned off. Some are carrier beams to generate input random

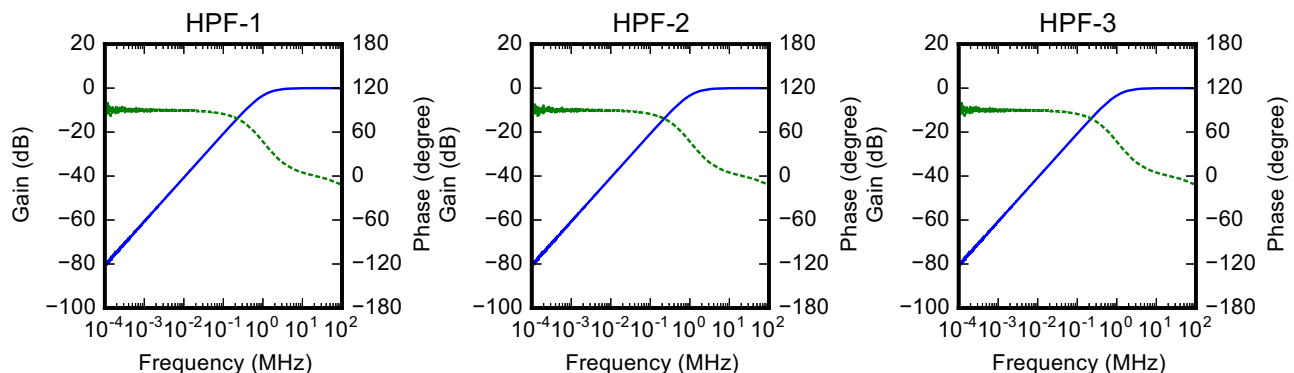


FIG. 6. Frequency characteristics of the HPFs, obtained by a network analyzer (Keysight, E5061B). Blue is gain, dotted green is phase.

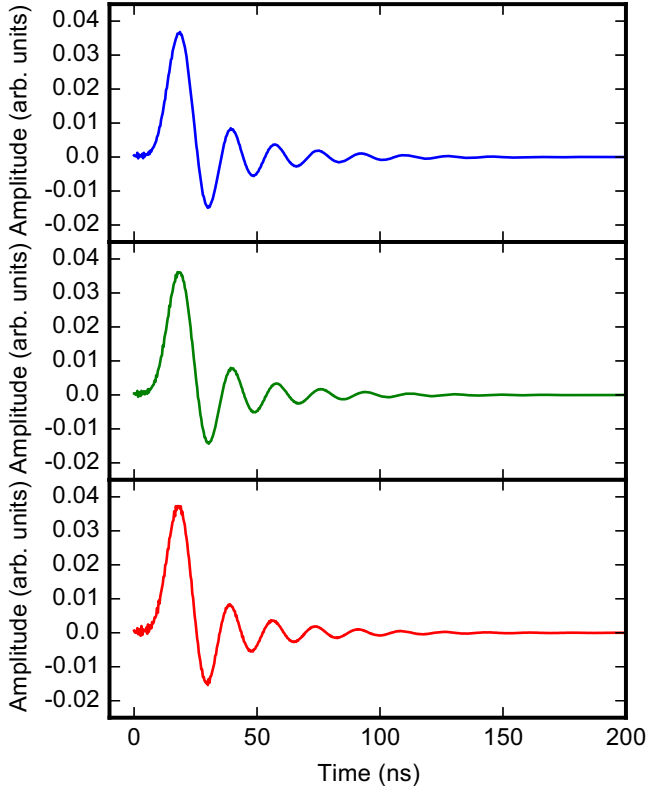


FIG. 7. Obtained response function of the LPF. Blue (top) shows LPF-1, green (middle) shows LPF-2, red (bottom) shows LPF-3.

signals by modulations, and others are carrier beams for feed-forward operations in the squeezing gates. The laser noise of these beams disturbs the homodyne signals. The noise by the input carrier beams is more significant than that by the feed-forward carrier beams because of the differences in optical path lengths. Since the input beams pass through the optical delay line before interference with the LOs, the phase noise looks larger in the output homodyne signals. This noise is filtered out by the HPF in Fig. 6 and thus they are not so significant problems, however, in order to further remove them, we employ procedures as follows:

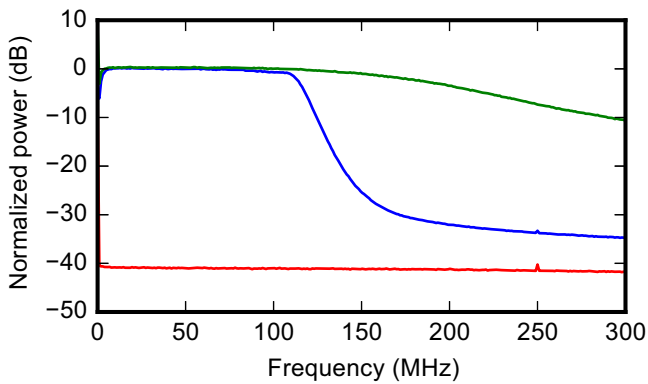


FIG. 8. Power spectrum of the input white signal. Green (top) shows unfiltered signal, blue (middle) shows filtered signal, red (bottom) shows oscilloscope noise floor.

The optical setup for the input random signal is shown in Fig. 11. For each of Input 1 and Input 2, three beams are used. Beam 1 is the phase reference for the QND gate. Beam 2 is the carrier beam to convert the random electronic signals to optical signals by phase modulation. While Beam 1 is temporally turned off during data acquisition, Beam 2 is always on. We use Beam 3, which is always on, for canceling the carrier component of Beam 2, leaving only the modulation sideband. Note that only Beam 1 is used when we use vacuum states as input states. The quadrature to add the random signal is selected via the relative phase between Beams 1 and 2. For example, for Input 1, when Beams 1 and 2 are locked in phase, the random signal is added to \hat{x}_1^{in} . On the other hand, when Beams 1 and 2 are locked 90° out of phase, the random signal is added to \hat{p}_1^{in} . Beam 3 is always locked to the opposite phase with Beam 2, removing the carrier component of Beam 2.

6. Feed-forward operation

The feed-forward operations in the squeezing gates cancel the antisqueezed noise of the ancillary squeezed vacua. Here we explain this by using equations. In the squeezing gate, first the input state (quadrature operators \hat{x}^{in} and \hat{p}^{in}) is coupled with an ancillary squeezed state (quadrature operators $\hat{x}^{(0)}e^{-r}$ and $\hat{p}^{(0)}e^r$ with a squeezing parameter r) by a beam splitter with a reflectivity R :

$$\hat{x}^{\text{int-1}} = \sqrt{R}\hat{x}^{\text{in}} + \sqrt{1-R}\hat{x}^{(0)}e^{-r}, \quad (\text{A1a})$$

$$\hat{p}^{\text{int-1}} = \sqrt{R}\hat{p}^{\text{in}} + \sqrt{1-R}\hat{p}^{(0)}e^r, \quad (\text{A1b})$$

$$\hat{x}^{\text{int-2}} = \sqrt{1-R}\hat{x}^{\text{in}} - \sqrt{R}\hat{x}^{(0)}e^{-r}, \quad (\text{A1c})$$

$$\hat{p}^{\text{int-2}} = \sqrt{1-R}\hat{p}^{\text{in}} - \sqrt{R}\hat{p}^{(0)}e^r. \quad (\text{A1d})$$

Next, as a feed-forward operation, the antisqueezed quadrature of a beam-splitter output $\hat{p}^{\text{int-2}}$ is measured and used for cancellation of the antisqueezed noise $\hat{p}^{(0)}e^r$ in the other output quadrature $\hat{p}^{\text{int-1}}$,

$$\hat{x}^{\text{out}} = \hat{x}^{\text{int-1}} = \sqrt{R}\hat{x}^{\text{in}} + \sqrt{1-R}\hat{x}^{(0)}e^{-r}, \quad (\text{A2a})$$

$$\hat{p}^{\text{out}} = \hat{p}^{\text{int-1}} + \sqrt{\frac{1-R}{R}}\hat{p}^{\text{int-2}} = \frac{1}{\sqrt{R}}\hat{p}^{\text{in}}. \quad (\text{A2b})$$

In the ideal limit of $r \rightarrow \infty$, the excess noise term $\hat{x}^{(0)}e^{-r}$ vanishes, and Eq. (A2b) approaches the ideal squeezing transformation where the squeezing degree is determined by the reflectivity R .

For the cancellation of the antisqueezed noise, unlike the previous narrowband experiments [17,18], the electronic signal for the feed-forward must be synchronized with the optical signal; in other words, the phase lags must be matched at all the frequencies. For this purpose, we use high-speed homodyne detectors and amplifiers with a flat gain and a linear dispersion, and the optical delay line for the compensation of the electronic delay. We confirmed the broadband cancellation by using a network analyzer (MS4630B, ANRITSU), which is shown in Figs. 12 and 13. Modulation signals are added by an EOM before the OPOs to the ancillary quadratures to be antisqueezed, and they are canceled by the feed-forward. Figures 12(a), 12(b), 13(a), and 13(b) are the gains and phases of the modulated reference beams through the optical delay

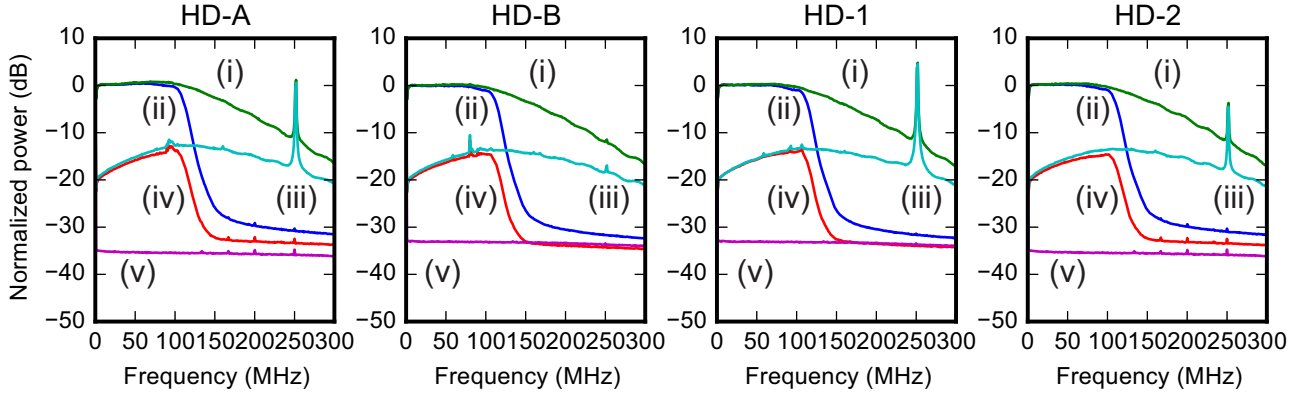


FIG. 9. Noise power spectra of four homodyne detectors. (i) Green shows optical shot noise spectra without the LPF. (ii) Blue shows optical shot noise spectra with the LPF. (iii) Cyan shows detector dark noise spectra without the LPF. (iv) Red shows detector dark noise spectra with the LPF. (v) Magenta shows oscilloscope noise floor.

line. The gains decrease at higher frequencies due to the bandwidth of the OPO cavities. They are used for calibration of the traces in the other figures in Figs. 12 and 13. Figures 12(c), 12(d), 13(c), and 13(d) are the gains and phases through the feed-forward electronic paths. The gains are flat and the phases are opposite (180°) for up to 100 MHz. Figures 12(e), 12(f), 13(e), and 13(f) are the residual modulation signals after the cancellation. The extinction ratios of the modulated signals are more than 20 dB for up to 100 MHz.

APPENDIX B: RESPONSE OF QUANTUM NONDEMOLITION GATE

1. General theory of response functions and cancellation

We consider a linear and static system

$$y(t) = \int f(t - \tau)w(\tau)d\tau + v(t), \tag{B1}$$

where $f(t)$ is a response function, $w(t)$ is an input signal, $y(t)$ is an output signal, and $v(t)$ is an excess noise which is independent of $w(t)$, i.e., the cross-correlation vanishes,

$$R_{wv}(t) = \langle w(\tau)v(\tau + t) \rangle = \int w(\tau)v(\tau + t)d\tau = 0. \tag{B2}$$

The response function $f(t)$ is obtained by deconvolution from the input-output cross correlation. The autocorrelation $R_{ww}(t)$ and the cross correlation $R_{wy}(t)$ are

$$R_{ww}(t) = \int w(\tau)w(\tau + t)d\tau, \tag{B3a}$$

$$R_{wy}(t) = \int w(\tau)y(\tau + t)d\tau = \iint w(\tau)w(\tau')f(\tau - \tau' + t)d\tau d\tau', \tag{B3b}$$

or in the frequency domain,

$$S_{ww}(\omega) = |W(\omega)|^2, \tag{B4a}$$

$$S_{wy}(\omega) = |W(\omega)|^2 F(\omega). \tag{B4b}$$

Therefore, the response function is obtained in the frequency domain by

$$F(\omega) = \frac{S_{wy}(\omega)}{S_{ww}(\omega)}. \tag{B5}$$

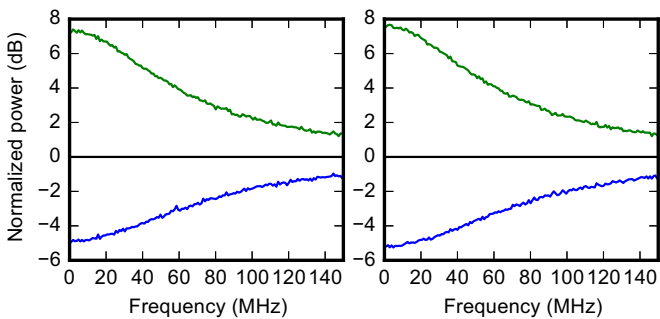


FIG. 10. Noise power spectra of ancillary squeezed vacua, normalized by the shot-noise spectrum. Green (upper) shows anti-squeezed quadrature. Blue (lower) shows squeezed quadrature.

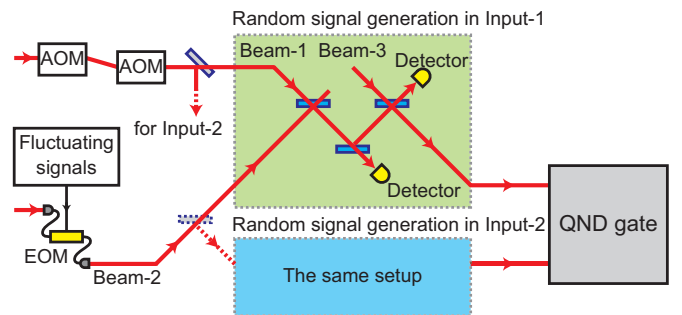


FIG. 11. Experimental setup for input signal preparation. Beam 2 is sent to either Input 1 or Input 2.

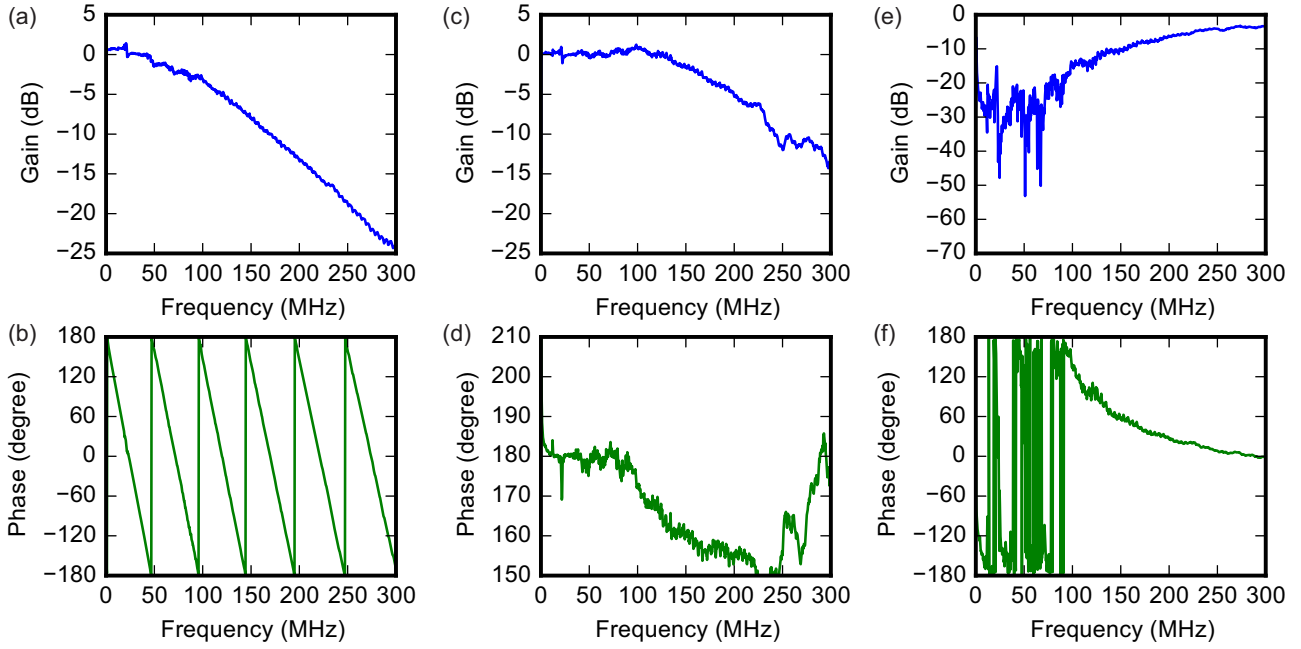


FIG. 12. Cancellation of the modulated signal by the feed-forward in the squeezing gate A. (a), (b) Gain and phase of the reference beam in the squeezing gate A, used for calibration of the other traces. (c), (d) Gain and phase of the feed-forward beam in the squeezing gate A. (e), (f) The results of the cancellation of the modulated signal.

The obtained response function $f(t)$ gives the optimal cancellation of the input signal, i.e.,

$$\left\langle \left[y(t) - \int h(t - \tau)w(\tau)d\tau \right]^2 \right\rangle = \langle v^2(t) \rangle + \left\langle \left[\int [f(t - \tau) - h(t - \tau)]w(\tau)d\tau \right]^2 \right\rangle, \quad (B6)$$

which is minimized when $h(t) = f(t)$. Note that the cross terms vanish by using Eq. (B2).

2. Experimental response functions

If the QND gate is not working instantaneously, the QND gate transformations in the time domain are generally in

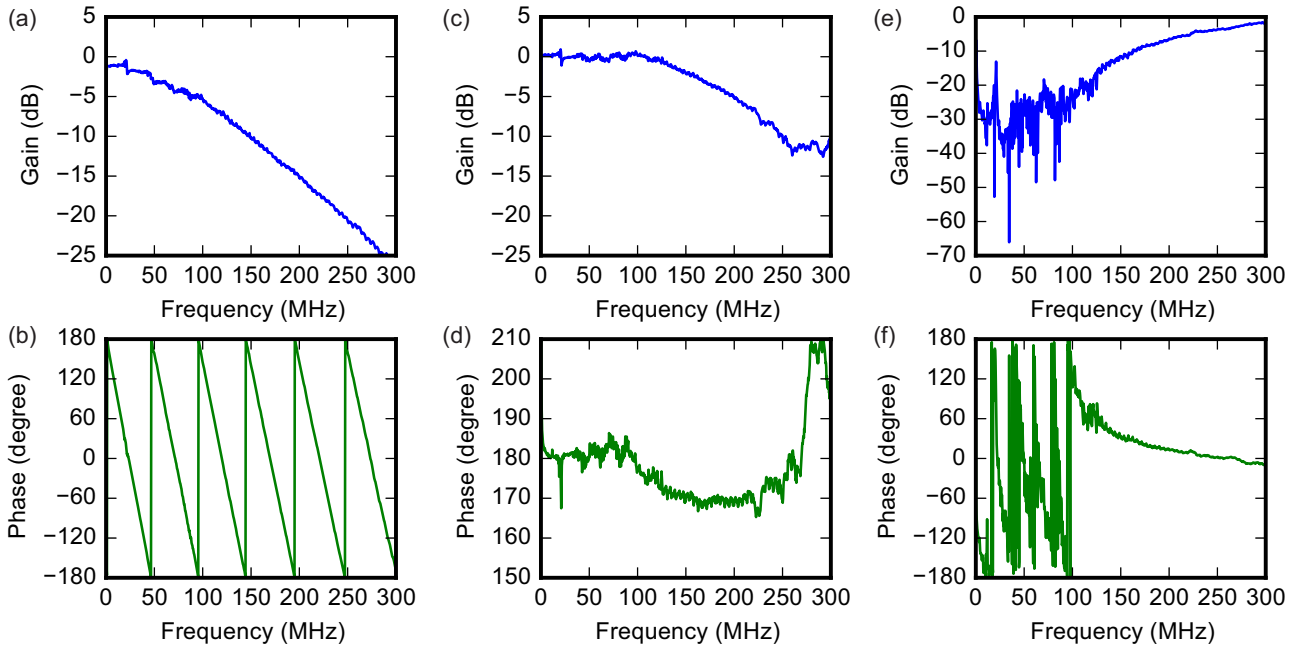


FIG. 13. Cancellation of the modulated signal by the feed-forward in the squeezing gate B. (a), (b) Gain and phase of the reference beam in the squeezing gate B, used for calibration of the other traces. (c), (d) Gain and phase of the feed-forward beam in the squeezing gate B. (e), (f) The results of the cancellation of the modulated signal.

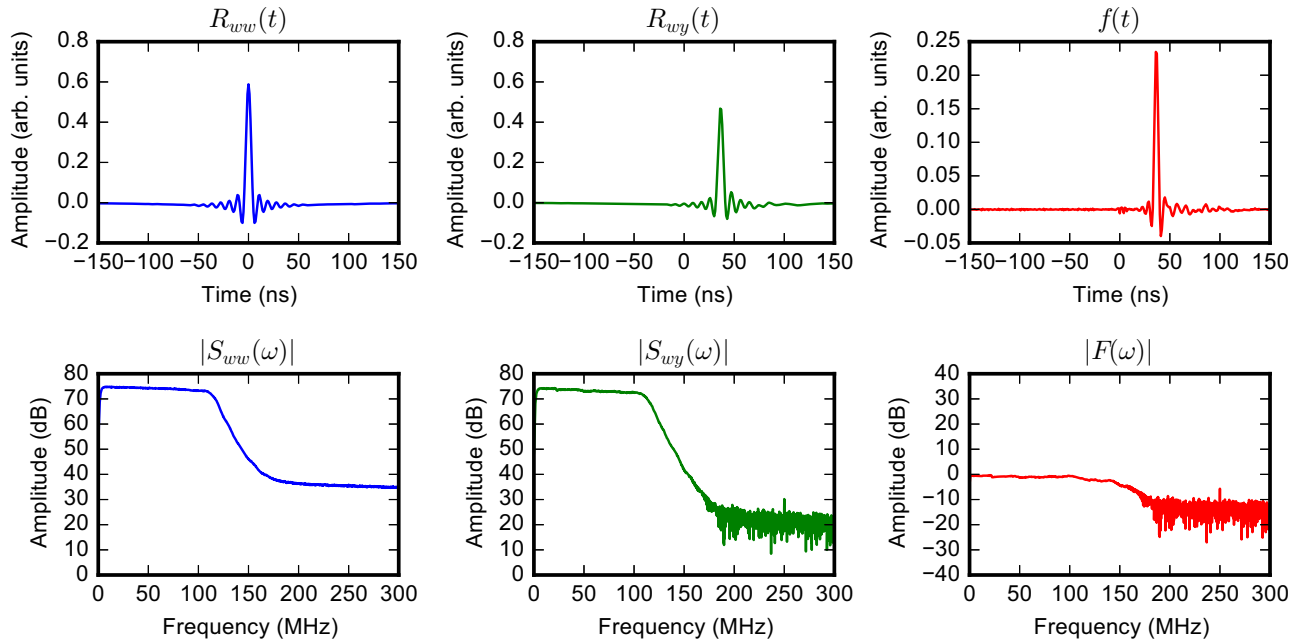


FIG. 14. Experimental input autocorrelation, input-output cross correlation, and response function $(f_{in \rightarrow 1} * f_{1 \rightarrow 1}^x * f_{1 \rightarrow out})(t)$ in the time domain (top panels) and in the frequency domain (bottom panels).

the form of

$$\hat{x}_1^{out}(t) = \int f_{1 \rightarrow 1}^x(t - \tau) \hat{x}_1^{in}(\tau) d\tau + \text{other noise terms}, \quad (B7a)$$

$$\hat{x}_2^{out}(t) = \int f_{1 \rightarrow 2}^x(t - \tau) \hat{x}_1^{in}(\tau) d\tau + \int f_{2 \rightarrow 2}^x(t - \tau) \hat{x}_2^{in}(\tau) d\tau + \text{other noise terms}, \quad (B7b)$$

$$\hat{p}_1^{out}(t) = \int f_{1 \rightarrow 1}^p(t - \tau) \hat{p}_1^{in}(\tau) d\tau - \int f_{2 \rightarrow 1}^p(t - \tau) \hat{p}_2^{in}(\tau) d\tau + \text{other noise terms}, \quad (B7c)$$

$$\hat{p}_2^{out}(t) = \int f_{2 \rightarrow 2}^p(t - \tau) \hat{p}_2^{in}(\tau) d\tau + \text{other noise terms}. \quad (B7d)$$

We want to apply the theory in Appendix B 1 to this QND system. For the estimation of the response functions, the random signals are used. As an example, we consider the case where a random signal $\alpha(t)$ is added to the vacuum fluctuation $\hat{x}_1^{(0)}(t)$ as

$$\hat{x}_1^{in}(t) = \hat{x}_1^{(0)}(t) + \alpha(t), \quad (B8)$$

and the other three quadratures are kept at vacuum levels. In this case, in theory, by examining the transfer of the random signal $\alpha(t)$ to the two output quadratures $\hat{x}_1^{out}(t)$ and $\hat{x}_2^{out}(t)$, response functions $f_{1 \rightarrow 1}^x(t)$ and $f_{1 \rightarrow 2}^x(t)$ are obtained, respectively. Note that the vacuum fluctuations, although they are white and random, cannot be used to estimate the response functions. As discussed in Appendix B 1, the important thing is that we know the input signal in order to obtain the cross correlation. In reality, we cannot obtain the response

functions with the procedures in Appendix B 1. The actual response functions obtained experimentally are $(f_{in \rightarrow k} * f_{k \rightarrow l}^{x,p} * f_{l \rightarrow out})(t)$, where $f_{in \rightarrow k}(t)$ is a response function of a conversion from an electronic signal to an optical signal, $f_{l \rightarrow out}(t)$ is a response function of a conversion from an optical signal to an electronic signal, and $*$ denotes a convolution.

As an example, we show the autocorrelation, the cross correlation, and the obtained response function $(f_{in \rightarrow 1} * f_{1 \rightarrow 1}^x * f_{1 \rightarrow out})(t)$ in Fig. 14. All the other experimentally estimated response functions from the input electronic signals to output the electronic signals are shown as traces (i)–(vi) in Fig. 15. All the response functions have the same shape. Note that, although we use LPFs and HPFs for output homodyne signals, the same filters are applied before the storage of the input signal as shown in Fig. 1(b) in the main text and thus the effect of the filters are canceled in the response functions. These response functions improve the cancellation in Fig. 3 in the main text. Figure 16 shows all the power spectra of cancellation with and without the response functions when the random signal is added to one of the four input quadratures \hat{x}_1^{in} , \hat{x}_2^{in} , \hat{p}_1^{in} , and \hat{p}_2^{in} . Black, red, magenta, blue, and green traces are the spectra for the shot noise as references, the QND outputs with vacuum inputs, those with the random signal input, the cancellation with the response functions, and the cancellation without them, respectively. The signals are perfectly canceled when the response functions are used, which means that the evolution of the signals through the QND gate is completely predictable.

However, we note that over-150-MHz components of the response functions do not actually represent the response of the QND gate but are determined by other reasons. For the frequencies higher than 150 MHz, the homodyne signals are highly attenuated by the LPF and thus electronic noise is dominant. While this electronic noise has a negligible cross

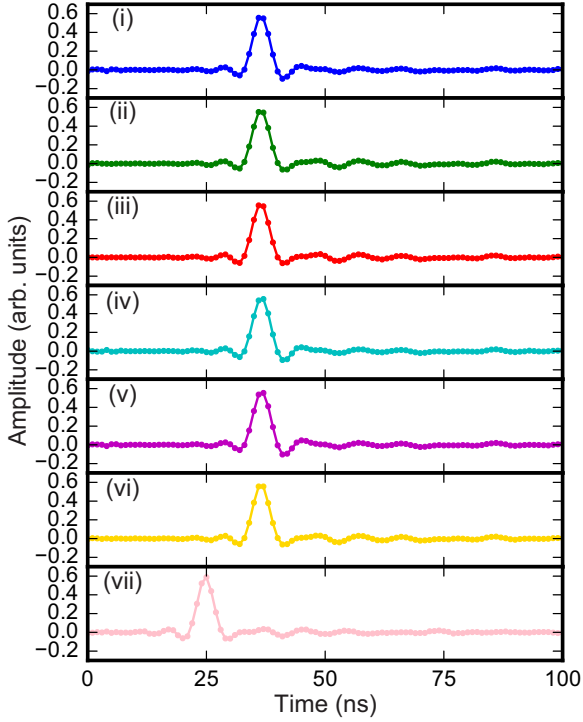


FIG. 15. Estimated response functions, used for the cancellation in Fig. 16. (i) $(f_{in \rightarrow 1} * f_{1 \rightarrow 1}^x * f_{1 \rightarrow out})(t)$. (ii) $(f_{in \rightarrow 1} * f_{1 \rightarrow 2}^x * f_{2 \rightarrow out})(t)$. (iii) $(f_{in \rightarrow 2} * f_{2 \rightarrow 2}^x * f_{2 \rightarrow out})(t)$. (iv) $(f_{in \rightarrow 1} * f_{1 \rightarrow 1}^p * f_{1 \rightarrow out})(t)$. (v) $(f_{in \rightarrow 2} * f_{2 \rightarrow 2}^p * f_{2 \rightarrow out})(t)$. (vi) $(f_{in \rightarrow 2} * f_{2 \rightarrow 2}^p * f_{2 \rightarrow out})(t)$. (vii) $(f_{in \rightarrow 1} * f_{1 \rightarrow out})(t)$.

correlation between channels, it contributes to the autocorrelation. Even though we subtracted the background electronic noise obtained without the optical LOs, there was still some residual noise, by which the denominator becomes much larger than the numerator in Eq. (B5) over 150 MHz. As a result, the response functions look as if they have a limited bandwidth of less than 150 MHz. The dull shape of the response functions shown in Fig. 15 are because of these situations.

To estimate the response function of the QND gate itself $f_{k \rightarrow l}^{x,p}(t)$, we conducted the following experiment. As references, we estimated the response functions $(f_{in \rightarrow 1} * f_{1 \rightarrow out})(t)$ for conversion of electric signals to optical signals and vice versa without the QND gate, and obtained a trace (vii) in Fig. 15. Here, we assumed negligible differences among peripheral response functions $(f_{in \rightarrow k} * f_{l \rightarrow out})(t)$. The trace (vii) has the same shape as those of the traces (i)–(vi) with a time difference of 11 ns. This time difference simply represents the difference of the positions of the homodyne detectors and does not directly represent the QND gate latency of about 13 ns corresponding to the optical path length of about 3.8 m. The response functions of the QND gate are obtained by the deconvolution of the traces (i)–(vi) by the trace (vii), and the results in the frequency domain are shown in Fig. 17. The obtained spectra are flat for up to 100 MHz, and thus we conclude that the response functions of the QND gate are like a δ function in the considered timescale. Inner products of all the traces (i)–(vii) in Fig. 15 with the time shift of 11 ns are summarized in Table I.

APPENDIX C: TRANSFER COEFFICIENTS AND CONDITIONAL VARIANCES

As discussed in Appendix B 2, the response of the QND gate is like a δ function in the considered timescale. Therefore, we can apply the conventional QND criteria [37] to the filtered quadrature values at each time, without considering a complicated mixing of quadratures at different times. Here, we summarize the QND criteria, especially, the connections between the QND quantities and the signal-to-noise ratios (SNRs).

General linear conversions of a signal observable \hat{A}_S and a probe observable \hat{A}_P by a nonideal QND gate are

$$\hat{A}_S^{\text{out}} = G_{S,S} \hat{A}_S^{\text{in}} + G_{S,P} \hat{A}_P^{\text{in}} + G_{S,NC} \hat{N}_{\text{COM}} + \hat{N}_S, \quad (\text{C1a})$$

$$\hat{A}_P^{\text{out}} = G_{P,S} \hat{A}_S^{\text{in}} + G_{P,P} \hat{A}_P^{\text{in}} + G_{P,NC} \hat{N}_{\text{COM}} + \hat{N}_P, \quad (\text{C1b})$$

where \hat{N}_{COM} is a correlated component, and \hat{N}_S and \hat{N}_P are uncorrelated components, of excess noise of the gate. The success criteria of the QND measurements are [37]

$$1 < T_S + T_P, \quad V_{S|P} < 1. \quad (\text{C2})$$

The transfer coefficients T_S , T_P and the conditional variance $V_{S|P}$ are defined as

$$T_S = C_{\hat{A}_S^{\text{in}} \hat{A}_S^{\text{out}}}^2 = \frac{|\langle \hat{A}_S^{\text{in}} \hat{A}_S^{\text{out}} \rangle - \langle \hat{A}_S^{\text{in}} \rangle \langle \hat{A}_S^{\text{out}} \rangle|^2}{V_{\hat{A}_S^{\text{in}}} V_{\hat{A}_S^{\text{out}}}}, \quad (\text{C3a})$$

$$T_P = C_{\hat{A}_S^{\text{in}} \hat{A}_P^{\text{out}}}^2 = \frac{|\langle \hat{A}_S^{\text{in}} \hat{A}_P^{\text{out}} \rangle - \langle \hat{A}_S^{\text{in}} \rangle \langle \hat{A}_P^{\text{out}} \rangle|^2}{V_{\hat{A}_S^{\text{in}}} V_{\hat{A}_P^{\text{out}}}}, \quad (\text{C3b})$$

$$\begin{aligned} V_{S|P} &= V_{\hat{A}_S^{\text{out}}} \left(1 - C_{\hat{A}_S^{\text{out}} \hat{A}_P^{\text{out}}}^2 \right) \\ &= V_{\hat{A}_S^{\text{out}}} \left(1 - \frac{V_{\hat{A}_S^{\text{out}} \hat{A}_P^{\text{out}}}}{V_{\hat{A}_S^{\text{out}}} V_{\hat{A}_P^{\text{out}}}} \right) \\ &= V_{\hat{A}_S^{\text{out}}} \left(1 - \frac{|\langle \hat{A}_S^{\text{out}} \hat{A}_P^{\text{out}} \rangle - \langle \hat{A}_S^{\text{out}} \rangle \langle \hat{A}_P^{\text{out}} \rangle|^2}{V_{\hat{A}_S^{\text{out}}} V_{\hat{A}_P^{\text{out}}}} \right), \end{aligned} \quad (\text{C3c})$$

where $V_{\hat{X}\hat{Y}}$, $V_{\hat{X}}$, and $C_{\hat{X}\hat{Y}}$ are a covariance, a variance, and a correlation, respectively,

$$V_{\hat{X}\hat{Y}} = \langle \hat{X}\hat{Y} \rangle - \langle \hat{X} \rangle \langle \hat{Y} \rangle, \quad (\text{C4a})$$

$$V_{\hat{X}} = V_{\hat{X}\hat{X}}, \quad (\text{C4b})$$

$$C_{\hat{X}\hat{Y}} = \frac{V_{\hat{X}\hat{Y}}}{\sqrt{V_{\hat{X}} V_{\hat{Y}}}}, \quad (\text{C4c})$$

and the signal input state is assumed to be a coherent state, $V_{\hat{A}_S^{\text{in}}} = 1$, i.e., the latter part of Eq. (C2) means that the signal observable is squeezed by the QND measurement. Note that the transfer coefficients and the conditional variance are $T_S = 1$, $T_P = G/(1+G)$, and $V_{S|P} = 1/(1+G^2)$, for the ideal QND interaction, $\hat{A}_S^{\text{out}} = \hat{A}_S^{\text{in}}$, $\hat{A}_P^{\text{out}} = G\hat{A}_S^{\text{in}} + \hat{A}_P^{\text{in}}$, with a coherent-state probe input $V_{\hat{A}_P^{\text{in}}} = 1$. The excess noise of the gate decreases the transfer coefficients and increase the conditional variance. With the general linear conversions in

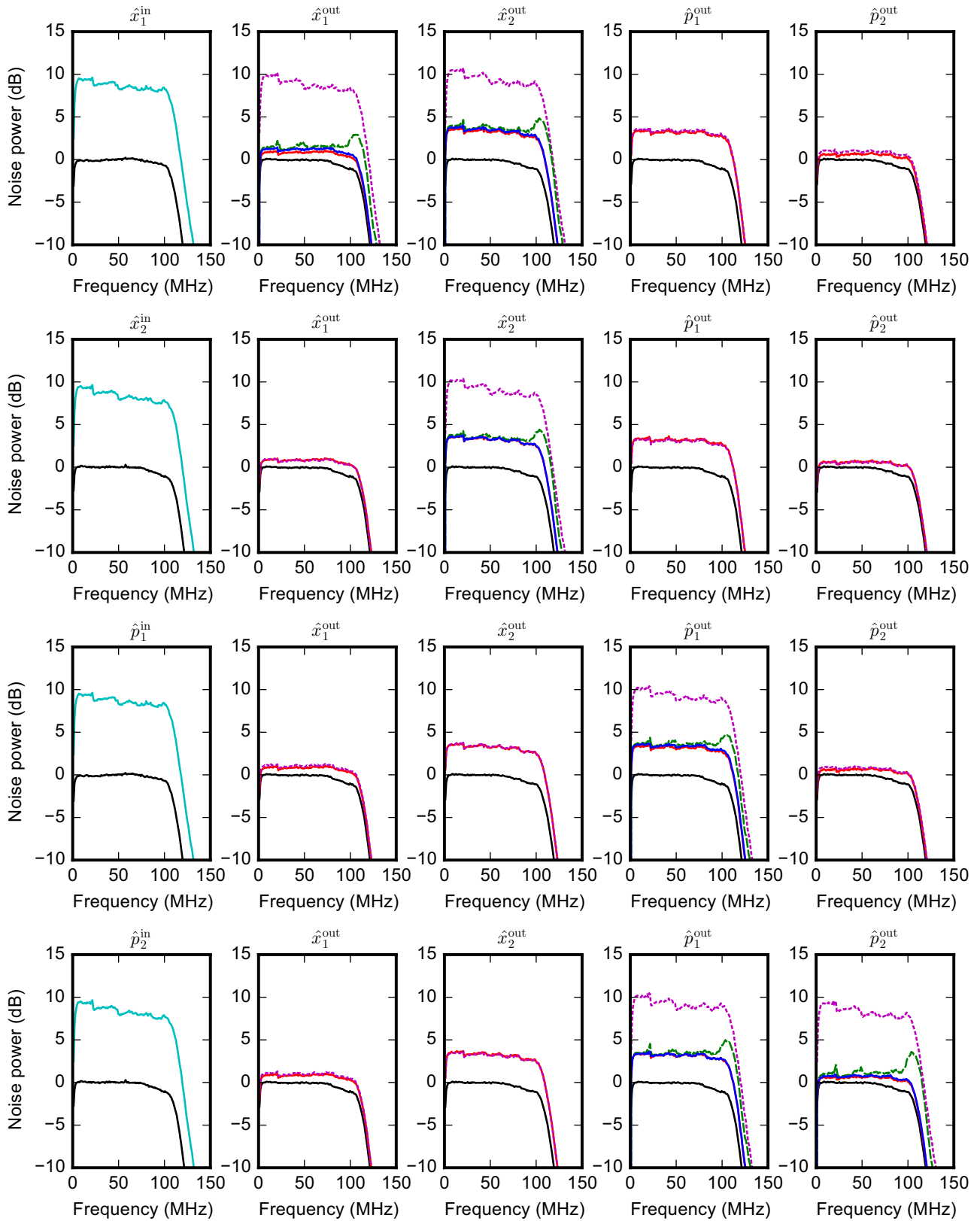


FIG. 16. Power spectra of all the cases where a random signal is added to one of the input quadratures \hat{x}_1^{in} , \hat{x}_2^{in} , \hat{p}_1^{in} , and \hat{p}_2^{in} . Black (bottom) shows shot noise. Red shows the QND outputs with vacuum-state inputs. Cyan (upper in left-end row) shows optical random signal at the input. Dotted magenta shows the QND outputs with the random signal input. Dashed green shows cancellation of the random signal without the response functions. Blue shows cancellation of the random signal with the response functions, which almost overlaps with red.

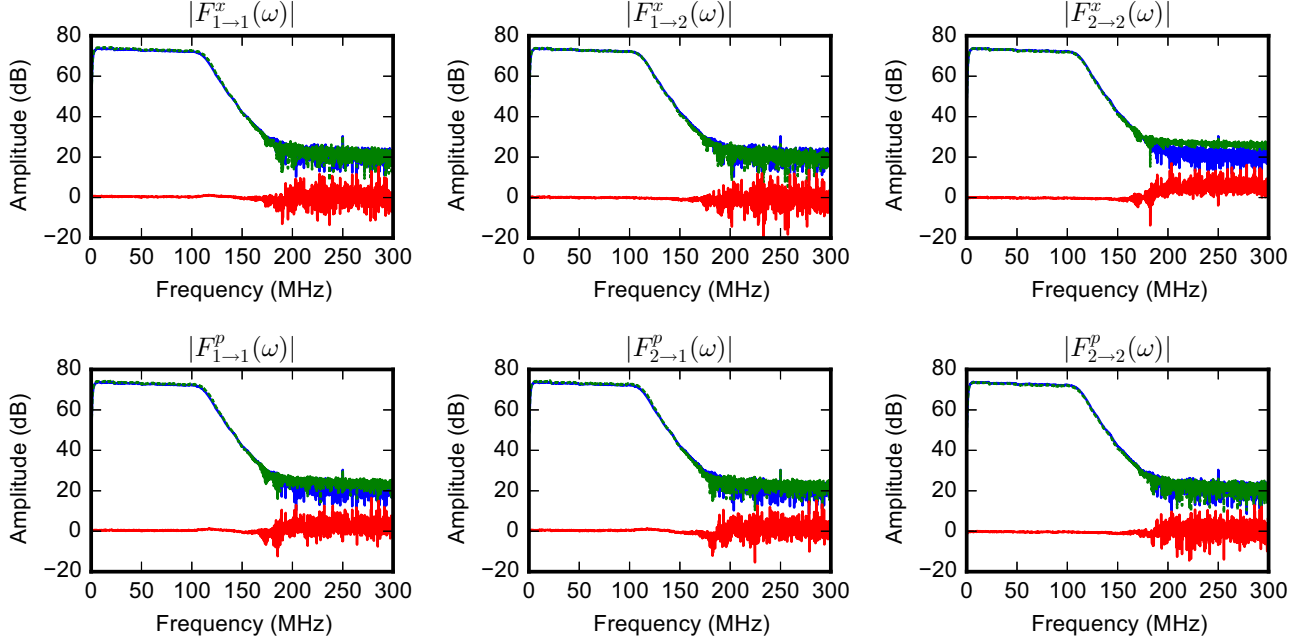


FIG. 17. Response functions of the QND gate in the frequency domain. Blue shows response function $|F_{\text{in} \rightarrow 1}(\omega)F_{1 \rightarrow \text{out}}(\omega)|$. Dotted green shows response functions $|F_{\text{in} \rightarrow 1}(\omega)F_{k \rightarrow l}^{x,p}(\omega)F_{1 \rightarrow \text{out}}(\omega)|$. Red (bottom) shows response functions $|F_{k \rightarrow l}^{x,p}(\omega)|$.

Eq. (C1), the transfer coefficients are

$$T_S = \frac{G_{S,S}^2 V_{\hat{A}_S^{\text{in}}}}{G_{S,S}^2 V_{\hat{A}_S^{\text{in}}} + G_{S,P}^2 V_{\hat{A}_P^{\text{in}}} + G_{S,NC}^2 V_{\hat{N}_{\text{COM}}} + V_{\hat{N}_S}}, \quad (\text{C5a})$$

$$T_P = \frac{G_{P,S}^2 V_{\hat{A}_S^{\text{in}}}}{G_{P,S}^2 V_{\hat{A}_S^{\text{in}}} + G_{P,P}^2 V_{\hat{A}_P^{\text{in}}} + G_{P,NC}^2 V_{\hat{N}_{\text{COM}}} + V_{\hat{N}_P}}, \quad (\text{C5b})$$

and the conditional variance is discussed later.

The transfer coefficients T_S and T_P are experimentally obtained by examining the transfer of the SNRs. For this purpose, we add a signal α to the signal input $\hat{A}_S^{\text{in}} = \delta \hat{A}_S^{\text{in}} + \alpha$, where $\delta \hat{A}_S^{\text{in}}$ is a vacuum noise fluctuation $\langle \delta \hat{A}_S^{\text{in}} \rangle = 0$, $V_{\delta \hat{A}_S^{\text{in}}} = 1$, and the power is compared with that of the case without the input signal $\hat{A}_S^{\text{in}} = \delta \hat{A}_S^{\text{in}}$. The SNR at the signal input is

$$\text{SNR}_S^{\text{in}} = \frac{\alpha^2}{V_{\hat{A}_S^{\text{in}}}} = \frac{\langle (\delta \hat{A}_S^{\text{in}} + \alpha)^2 \rangle - \langle (\delta \hat{A}_S^{\text{in}})^2 \rangle}{\langle (\delta \hat{A}_S^{\text{in}})^2 \rangle}, \quad (\text{C6})$$

and thus obtained experimentally from the powers of the two cases $\langle (\delta \hat{A}_S^{\text{in}} + \alpha)^2 \rangle$ and $\langle (\delta \hat{A}_S^{\text{in}})^2 \rangle$. On the other hand, the

TABLE I. Inner products between all the response functions (i)–(vii) in Fig. 15.

Response function	(i)	(ii)	(iii)	(iv)	(v)	(vi)	(vii)
(i)	1	0.989	0.991	0.990	0.994	0.990	0.976
(ii)		1	0.989	0.990	0.988	0.995	0.978
(iii)			1	0.985	0.986	0.990	0.972
(iv)				1	0.992	0.991	0.982
(v)					1	0.989	0.982
(vi)						1	0.981
(vii)							1

output signal and probe observables become $\hat{A}_S^{\text{out}} = \delta \hat{A}_S^{\text{out}} + G_{S,S}\alpha$ and $\hat{A}_P^{\text{out}} = \delta \hat{A}_P^{\text{out}} + G_{P,S}\alpha$, where $\delta \hat{A}_S^{\text{out}}$ and $\delta \hat{A}_P^{\text{out}}$ are noise fluctuations without the input signal α . We assume $\langle \delta \hat{A}_S^{\text{out}} \rangle = \langle \delta \hat{A}_P^{\text{out}} \rangle = 0$ without loss of generality. The SNRs at the signal and probe outputs are

$$\begin{aligned} \text{SNR}_S^{\text{out}} &= \frac{G_{S,S}^2 \alpha^2}{V_{\hat{A}_S^{\text{out}}}} = \frac{\langle (\delta \hat{A}_S^{\text{out}} + G_{S,S}\alpha)^2 \rangle - \langle (\delta \hat{A}_S^{\text{out}})^2 \rangle}{\langle (\delta \hat{A}_S^{\text{out}})^2 \rangle} \\ &= \frac{G_{S,S}^2 \alpha^2}{G_{S,S}^2 V_{\hat{A}_S^{\text{in}}} + G_{S,P}^2 V_{\hat{A}_P^{\text{in}}} + G_{S,NC}^2 V_{\hat{N}_{\text{COM}}} + V_{\hat{N}_S}}, \end{aligned} \quad (\text{C7a})$$

$$\begin{aligned} \text{SNR}_P^{\text{out}} &= \frac{G_{P,S}^2 \alpha^2}{V_{\hat{A}_P^{\text{out}}}} = \frac{\langle (\delta \hat{A}_P^{\text{out}} + G_{P,S}\alpha)^2 \rangle - \langle (\delta \hat{A}_P^{\text{out}})^2 \rangle}{\langle (\delta \hat{A}_P^{\text{out}})^2 \rangle} \\ &= \frac{G_{P,S}^2 \alpha^2}{G_{P,S}^2 V_{\hat{A}_S^{\text{in}}} + G_{P,P}^2 V_{\hat{A}_P^{\text{in}}} + G_{P,NC}^2 V_{\hat{N}_{\text{COM}}} + V_{\hat{N}_S}}, \end{aligned} \quad (\text{C7b})$$

and thus obtained experimentally from the powers of the two cases $\langle (\delta \hat{A}_S^{\text{out}} + G_{S,S}\alpha)^2 \rangle$, $\langle (\delta \hat{A}_P^{\text{out}} + G_{P,S}\alpha)^2 \rangle$ and $\langle (\delta \hat{A}_S^{\text{out}})^2 \rangle$, $\langle (\delta \hat{A}_P^{\text{out}})^2 \rangle$. By using Eqs. (C5)–(C7), we obtain

$$T_S = \frac{\text{SNR}_S^{\text{out}}}{\text{SNR}_S^{\text{in}}}, \quad T_P = \frac{\text{SNR}_P^{\text{out}}}{\text{SNR}_S^{\text{in}}}. \quad (\text{C8})$$

Therefore, T_S and T_P represent the degradation of the SNR when the signal input α is transferred to the signal and probe outputs, respectively.

The conditional variance $V_{S|P}$ corresponds to the minimum variance of $\hat{A}_S^{\text{out}} - g\hat{A}_P^{\text{out}}$ where the subtraction gain g is an optimization parameter. The variance of $\hat{A}_S^{\text{out}} - g\hat{A}_P^{\text{out}}$ is a

TABLE II. Verification of transfer coefficients in the QND gate. The coherent-state amplitude is injected either to x_1^{in} or p_2^{in} .

Coherent state input	x_1^{in}	p_2^{in}
T_S	0.86 ± 0.02	0.85 ± 0.02
T_P	0.51 ± 0.01	0.52 ± 0.01
$T_S + T_P$	1.37 ± 0.03	1.37 ± 0.03
$V_{\text{S P}}$	0.88 ± 0.01	0.88 ± 0.01

quadratic polynomial in g ,

$$\begin{aligned}
 V_{\hat{A}_S^{\text{out}} - g\hat{A}_P^{\text{out}}} &= \langle (\delta\hat{A}_S^{\text{out}} - g\delta\hat{A}_P^{\text{out}})^2 \rangle \\
 &= V_{\hat{A}_P^{\text{out}}} g^2 - 2V_{\hat{A}_S^{\text{out}} \hat{A}_P^{\text{out}}} g + V_{\hat{A}_S^{\text{out}}} \\
 &= V_{\hat{A}_P^{\text{out}}} \left(g - \frac{V_{\hat{A}_S^{\text{out}} \hat{A}_P^{\text{out}}}}{V_{\hat{A}_P^{\text{out}}}} \right)^2 + V_{\text{S|P}}, \quad (\text{C9})
 \end{aligned}$$

which is minimized at $g = V_{\hat{A}_S^{\text{out}} \hat{A}_P^{\text{out}}} / V_{\hat{A}_P^{\text{out}}}$.

The experimental values are summarized in Table II. The variances $\langle (\hat{x}_1^{\text{out}} - g_x \hat{x}_2^{\text{out}})^2 \rangle$ and $\langle (g_p \hat{p}_1^{\text{out}} + \hat{p}_2^{\text{out}})^2 \rangle$ for various subtraction and addition gains are plotted in Fig. 18.

APPENDIX D: QUANTUM ENTANGLEMENT

The sub-shot-noise conditional variances $V_{\text{S|P}} < 1$ in both of the \hat{x} and \hat{p} quadratures are not a sufficient condition for entanglement. A sufficient condition based on the Duan-Simon criterion is [17,39,40]

$$\exists g, \langle (\hat{x}_1^{\text{out}} - g\hat{x}_2^{\text{out}})^2 \rangle + \langle (g\hat{p}_1^{\text{out}} + \hat{p}_2^{\text{out}})^2 \rangle < 4|g|. \quad (\text{D1})$$

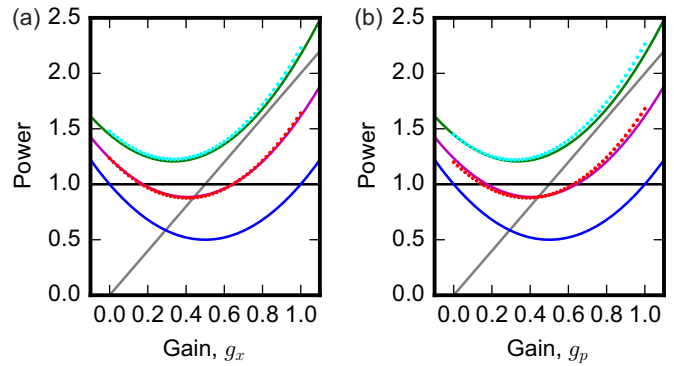


FIG. 18. Normalized variances (dimensionless) of (a) $\hat{x}_1^{\text{out}} - g_x \hat{x}_2^{\text{out}}$ and (b) $g_p \hat{p}_1^{\text{out}} + \hat{p}_2^{\text{out}}$. Cyan (upper) markers show experimental results when ancillary squeezed vacua are not used. Red (lower) markers show experimental results when ancillary squeezed vacua are used. Green (top) curves show theoretical variance when ancillary squeezed vacua are not used. Magenta (middle) curves show theoretical variance when ancillary squeezed vacua with -2.8 dB of squeezing are used. Blue (bottom) curves show theoretical variance for the ideal QND interaction with $G = 1$. Gray lines show entangled criterion.

In Fig. 18, there are gray lines $\langle (\hat{x}_1^{\text{out}} - g\hat{x}_2^{\text{out}})^2 \rangle = 2|g|$ and $\langle (g\hat{p}_1^{\text{out}} + \hat{p}_2^{\text{out}})^2 \rangle = 2|g|$, and there is a region of g where red markers are below the gray lines in both quadratures. Therefore, the two output modes are entangled for coherent-state inputs.

- [1] N. C. Menicucci, X. Ma, and T. C. Ralph, *Phys. Rev. Lett.* **104**, 250503 (2010).
- [2] N. C. Menicucci, *Phys. Rev. A* **83**, 062314 (2011).
- [3] S. Yokoyama, R. Ukai, S. C. Armstrong, C. Sornphiphatpong, T. Kaji, S. Suzuki, J. Yoshikawa, H. Yonezawa, N. C. Menicucci, and A. Furusawa, *Nat. Photon.* **7**, 982 (2013).
- [4] J. Yoshikawa, S. Yokoyama, T. Kaji, C. Sornphiphatpong, Y. Shiozawa, K. Makino, and A. Furusawa, *APL Photon.* **1**, 060801 (2016).
- [5] D. Gottesman, A. Kitaev, and J. Preskill, *Phys. Rev. A* **64**, 012310 (2001).
- [6] V. B. Braginsky, and F. Ya. Khalili, *Quantum Measurement* (Cambridge University Press, Cambridge, England, 1992).
- [7] S. F. Pereira, Z. Y. Ou, and H. J. Kimble, *Phys. Rev. Lett.* **72**, 214 (1994).
- [8] P. Grangier, J. A. Levenson, and J.-P. Poizat, *Nature (London)* **396**, 537 (1998).
- [9] S. L. Braunstein, *Phys. Rev. Lett.* **80**, 4084 (1998).
- [10] S. Lloyd and Jean-Jacques E. Slotine, *Phys. Rev. Lett.* **80**, 4088 (1998).
- [11] J. I. Cirac and H. J. Kimble, *Nat. Photon.* **11**, 18 (2017).
- [12] B. M. Terhal and D. Weigand, *Phys. Rev. A* **93**, 012315 (2016).
- [13] K. Fukui, A. Tomita, and A. Okamoto, *Phys. Rev. Lett.* **119**, 180507 (2017).
- [14] K. Fukui, A. Tomita, A. Okamoto, and K. Fujii, *Phys. Rev. X* **8**, 021054 (2018).
- [15] P. Marek, R. Filip, H. Ogawa, A. Sakaguchi, S. Takeda, J. Yoshikawa, and A. Furusawa, *Phys. Rev. A* **97**, 022329 (2018).
- [16] R. Filip, P. Marek, and U. L. Andersen, *Phys. Rev. A* **71**, 042308 (2005).
- [17] J. Yoshikawa, Y. Miwa, A. Huck, U. L. Andersen, P. van Loock, and A. Furusawa, *Phys. Rev. Lett.* **101**, 250501 (2008).
- [18] R. Ukai, S. Yokoyama, J. Yoshikawa, P. van Loock, and A. Furusawa, *Phys. Rev. Lett.* **107**, 250501 (2011).
- [19] S. Yokoyama, R. Ukai, J. Yoshikawa, P. Marek, R. Filip, and A. Furusawa, *Phys. Rev. A* **90**, 012311 (2014).
- [20] H. Ogawa, H. Ohdan, K. Miyata, M. Taguchi, K. Makino, H. Yonezawa, J. Yoshikawa, and A. Furusawa, *Phys. Rev. Lett.* **116**, 233602 (2016).
- [21] A. I. Lvovsky, H. Hansen, T. Aichele, O. Benson, J. Mlynek, and S. Schiller, *Phys. Rev. Lett.* **87**, 050402 (2001).
- [22] J. S. Neergaard-Nielsen, B. M. Nielsen, H. Takahashi, A. I. Vistnes, and E. S. Polzik, *Opt. Express* **15**, 7940 (2007).
- [23] A. Ourjoumtsev, R. Tualle-Broui, J. Laurat, and P. Grangier, *Science* **312**, 83 (2006).
- [24] J. S. Neergaard-Nielsen, B. M. Nielsen, C. Hettich, K. Mølmer, and E. S. Polzik, *Phys. Rev. Lett.* **97**, 083604 (2006).
- [25] S. D. Bartlett, B. C. Sanders, S. L. Braunstein, and K. Nemoto, *Phys. Rev. Lett.* **88**, 097904 (2002).

- [26] S. Lloyd and S. L. Braunstein, *Phys. Rev. Lett.* **82**, 1784 (1999).
- [27] N. Lee, H. Benichi, Y. Takeno, S. Takeda, J. Webb, E. Huntington, and A. Furusawa, *Science* **332**, 330 (2011).
- [28] S. Takeda, T. Mizuta, M. Fuwa, P. van Loock, and A. Furusawa, *Nature (London)* **500**, 315 (2013).
- [29] Y. Miwa, J. Yoshikawa, N. Iwata, M. Endo, P. Marek, R. Filip, P. van Loock, and A. Furusawa, *Phys. Rev. Lett.* **113**, 013601 (2014).
- [30] K. Miyata, H. Ogawa, P. Marek, R. Filip, H. Yonezawa, J. Yoshikawa, and A. Furusawa, *Phys. Rev. A* **90**, 060302(R) (2014).
- [31] M. Fuwa, S. Toba, S. Takeda, P. Marek, L. Mišta, Jr., R. Filip, P. van Loock, J. Yoshikawa, and A. Furusawa, *Phys. Rev. Lett.* **113**, 223602 (2014).
- [32] S. Takeda, M. Fuwa, P. van Loock, and A. Furusawa, *Phys. Rev. Lett.* **114**, 100501 (2015).
- [33] J. Zhang and S. L. Braunstein, *Phys. Rev. A* **73**, 032318 (2006).
- [34] S. Takeda and A. Furusawa, *Phys. Rev. Lett.* **119**, 120504 (2017).
- [35] M. M. Wilde, H. Krovi, and T. A. Brun, *Phys. Rev. A* **75**, 060303(R) (2007).
- [36] S. L. Braunstein, *Phys. Rev. A* **71**, 055801 (2005).
- [37] M. J. Holland, M. J. Collett, D. F. Walls, and M. D. Levenson, *Phys. Rev. A* **42**, 2995 (1990).
- [38] T. Serikawa, J. Yoshikawa, K. Makino, and A. Furusawa, *Opt. Express* **24**, 28383 (2016).
- [39] L.-M. Duan, G. Giedke, J. I. Cirac, and P. Zoller, *Phys. Rev. Lett.* **84**, 2722 (2000).
- [40] R. Simon, *Phys. Rev. Lett.* **84**, 2726 (2000).